Volume 1 | Number 1 | Jan 2013 | Pages 1–100

Journal of
Materials Chemistry A

Materials for energy and sustainability
www.rsc.org/materialsA

Li⁺

ROYAL SOCIETY
OF CHEMISTRY

ROYAL SOCIETY
OF CHEMISTRY

www.rsc.org/materialsA

Journal Name

ARTICLE

Mg-Fe-Al-O for advanced CO_2 to CO conversion: carbon monoxide yield vs. oxygen storage capacity

N. V. R. Aditya Dharanipragada[a], Lukas C. Buelens[a], Hilde Poelman[a], Eddy De Grave[b], Vladimir V. Galvita[a*] and Guy B. Marin[a]

Abstract: A detailed study of new oxygen carrier materials Mg-Fe-Al-O with various loadings of iron oxide (10 - 100wt% Fe_2O_3) is carried out in order to investigate the relationship between material transformation, stability and CO yield from CO_2 conversion. In situ XRD during H_2-TPR, CO_2-TPO and isothermal chemical looping cycles as well as Mössbauer spectroscopy are employed. All samples show the formation of a spinel phase $MgFeAlO_x$. High loadings of iron oxide (50-90wt%) lead to both spinel and Fe_2O_3 phases and show deactivation in cycling as a result of Fe_2O_3 particle sintering. During the reduction, reoxidation and cycling of the spinel $MgFeAlO_x$ phase, only limited sintering occurs. This is evidenced by the stable spinel crystallite sizes (~15-20nm) during isothermal cycling. The reduction of $MgFe^{3+}AlO_x$ starts at 400°C and proceeds via partial reduction to $MgFe^{2+}AlO_x$. Prolonged cycling and higher temperature (>750°C) lead to deeper reduction and segregation of Fe from the spinel structure. Very high stability and CO yield from CO_2 conversion is found in a Mg-Fe-Al-O material with 10wt% Fe_2O_3, i.e. the lowest oxygen storage capacity among the tested samples. Compared to 10wt% Fe_2O_3 supported on Al_2O_3 or MgO, the CO yield of the 10wt% Fe_2O_3-$MgFeAlO_x$ spinel is ten times higher.

1. Introduction

The contribution of carbon dioxide (CO_2) towards the greenhouse effect is well known[1, 2]. As suggested by the Intergovernmental Panel on Climate Control, a 50−85% reduction in total CO_2 emission by 2050 is necessary to limit the anticipated global temperature rise to 2°C[3]. Several alternative technologies have been proposed to mitigate the rising levels of CO_2 in the atmosphere. Most of the technologies which have the capability of reducing CO_2 emissions have a high energy penalty resulting in a reduction of their energy efficiency and an increase in the energy price. Thus, great efforts have been made during the last years to develop new low-cost carbon capture and storage technologies. Among these, chemical looping processes for carbon separation, capture and utilization are considered promising. They allow intrinsic separation of pure CO_2 from hydrocarbon combustion and enable its conversion into CO or syngas[4-9]. Chemical looping is a general term given to a process of transporting oxygen by means of a solid material which is used as oxygen carrier for the conversion of fuel. It is a cyclic process based on the periodic reduction and reoxidation of e.g. transition metal oxides which act as oxygen storage materials[9-

[11]. During the reduction phase, a gas reduces these metal oxides, thereby producing CO_2 and/or H_2O. In the reoxidation phase, carbon dioxide and/or steam are conducted to the reactor and reoxidize the oxygen storage materials hereby producing CO and/or H_2. Chemical looping CO_2 conversion utilizes more CO_2 than it produces in the reduction step[6, 12-15] when methane or biogas is used as reducing agent. Hence, this process can be one of the possible target technologies for CO_2 conversion and its advantage lies in its simplicity, as it can be carried out in one single reactor without any additional post processing steps.

The process economics are governed by the redox activity and stability of the transition metal oxides. Among the latter, iron oxides hold great promise due to their environmental compatibility and abundant availability, when compared to their counterparts (Cu, Ni, Mn, Co)[16-18]. However, pure iron oxide deactivates rapidly due to sintering. In an attempt to eliminate sintering, the use of promoter materials such as CeO_2, $CeZrO_2$, SiO_2, Al_2O_3, MgO and $MgAl_2O_4$ was proposed by several investigators[12, 19-25]. These promoters prevent sintering of the active material by either taking part in the reaction along with iron oxides or/and acting as a physical barrier during reaction[26]. Promoters like CeO_2 and $CeZrO_2$ contribute towards the reaction with their redox properties, while additionally forming thermally stable solid solutions. The success of the materials depends greatly on the solid-solid transformation occurring during the reaction. At the typical operating conditions of chemical looping, 700-900°C, structural transformations between the phases, leading to spinel formation, are inevitable. The different spinels like Fe_2SiO_4, $FeAl_2O_4$ and $Mg_{1-x}Fe_xO_{1-x}$

[a.] Laboratory for Chemical Technology, Ghent University, Technologiepark 914, B-9052, Ghent, Belgium;Tel: +32 93311722; E-mail: vladimir.galvita@UGent.be
[b.] Department of Physics and Astronomy, Ghent University, Proeftuinstraat 86, 9000, Belgium

formed during the reaction contribute towards stability by preventing sintering during prolonged cycling. However, spinel formation generally also leads to higher reduction temperatures and decreased oxygen storage capacity of the promoted iron oxides[27, 28].

A previous study, focusing on the redox properties of Fe_2O_3 with Al_2O_3 during prolonged H_2O and CO_2 splitting via chemical looping, revealed that both sintering and phase transformations contribute towards deactivation during the isothermal cycling process[29]. Sintering was the predominant cause of deactivation for materials with Al_2O_3 loadings less than 30wt%, at a cycling temperature of $650°C$. On the other hand, phase transformation to $FeAl_2O_4$ was mainly observed at higher loadings and at an operating temperature of $750°C$. These structural changes modified the redox properties of the materials but also contributed towards increased stability. During CO_2 and H_2O splitting over 100 cycles, the materials where the $FeAl_2O_4$ formation was intense showed stable operation, while materials with lower Al_2O_3 loadings, where $FeAl_2O_4$ was not predominant, sintered continuously leading to rapid deactivation upon cycling. The modified materials' properties, in particular the higher reduction temperature of the spinel $FeAl_2O_4$, contributed towards its stability which eventually proved beneficial to the reaction, even though the material had a lower oxygen storage capacity. Hence, apart from oxygen storage capacity, structural stability and repeated reducibility contribute towards high redox activity and are of equal importance in the design of oxygen storage materials.

In order to address the redox activity and stability of Al_2O_3 modified iron oxide, Mg-Fe-Al-O is suggested here as new oxygen storage material. The combination of Al^{3+}, Fe^{3+} and Mg^{2+} nitrates results after calcination in the formation of a $MgFeAlO_x$ spinel. It allows limited interaction of Fe_2O_3 with Mg-Al-O as only a fixed amount of Fe is incorporated in the spinel lattice. The formation of $MgFeAlO_x$ is usually the result of substitution of Al^{3+} with Fe^{3+} in $MgAlO_x$ which leads to stabilization and enhancement of reducibility properties[30, 31].

In the context of chemical looping, pure $MgAl_2O_4$ based materials have been extensively applied[32-35]. Fe_2O_3 supported on inert $MgAl_2O_4$ proved to perform well as oxygen carrier both for chemical looping combustion and for the steam–iron reaction[36, 37]. The spinel $MgFeAlO_x$ has also been applied previously, in processes like ethyl benzene dehydrogenation and removal of pollutants like SO_x[38, 39]. The behaviour of mixed materials Mg-Fe-Al-O in chemical looping and the role of their structural transformation has not been investigated, to the best of our knowledge. Hence, a detailed study was undertaken to establish a structure-property relationship and find a link between product yield and oxygen storage capacity for a series of Mg-Fe-Al-O, with varying loading of iron. The Mg-Fe-Al-O materials, prepared by co-precipitation, are investigated for the conversion of CO_2 in a chemical looping process. Experimental performance data are reported as well as structural characterization of the Mg-Fe-Al-O materials during reduction and reoxidation.

2. Experimental

2.1. Preparation of oxygen storage material

Mg-Fe-Al-O materials were prepared in a one pot synthesis with varying loadings of Fe_2O_3 (10, 20, 30, 50, 70, 80, 90 and 100wt%). Also, to compare the effect of different promoters, similar loadings of Fe_2O_3 with Al_2O_3 and MgO were synthesized. The following chemicals were used in the preparation of the mixed oxides: $Fe(NO_3)_3.9H_2O$ (99.99+%, Sigma-Aldrich®), $Mg(NO_3)_2.6H_2O$ (99.99%, Sigma-Aldrich®), $Al(NO_3)_3.9H_2O$ (98%, Sigma-Aldrich®). All samples were prepared via co-precipitation by ammonium hydroxide. The precipitate was then separated by filtration, followed by drying in an oven at 120°C for 14 hours. The resulting samples were calcined at 750°C for 6 hours. Samples are labelled as X-Mg-Fe-Al-O, where X represents the equivalent Fe_2O_3 wt% content as determined from ICP.

2.2. Material characterization

The Brunauer−Emmett−Teller (BET) surface area was determined by N_2 adsorption at -196°C (five point BET method using Gemini Micromeritics). The crystallographic phases of the as prepared materials were determined using a Siemens Diffractometer Kristalloflex D5000, with Cu Kα radiation. The powder patterns were collected in a 2θ range from 10° to 80° with a step of 0.02° and 30s counting time per angle. The crystallite size was determined using the Scherrer equation by fitting a Gaussian function to the four most intense characteristic peaks of each compound to obtain the peak widths[40].

The bulk chemical composition of the as prepared samples was determined by inductively Coupled Plasma – Atomic Emission Spectroscopy (ICP-AES) on an ICAP 6500 of Thermo Scientific. The ICP samples were mineralized by alkaline fusion with a mix of Li-tetraborate and Li-metaborate. Mössbauer spectra at -196°C were collected for sample 30-Mg-Fe-Al-O in as prepared state and after several treatments using a spectrometer operating in constant acceleration mode with triangular reference signal and a $^{57}Co(Rh)$ source. The counts were accumulated in 1024 channels. Spectra were run until an off-resonance count rate of at least 10^6 per channel was reached. The spectrometers were calibrated by collecting the RT spectrum of a reference metallic-iron foil or a standard α-Fe_2O_3 powder, depending on the applied velocity range. Isomer shifts quoted hereafter are referenced with respect to α-Fe at room temperature. The spectra were fitted with symmetrical Lorentzian-shaped sextets and/or doublets.

SEM images were acquired with a FEI Quanta 200F setup with a field emission electron source for high resolution imaging and beam stability. The EDX analysis in SEM was performed using EDAX Genesis 4000.

The redox behaviour of the different samples was investigated using H_2-TPR, CO_2-TPO and isothermal cycling in an Autochem II 2920, Micromeritics setup. About 30 mg of sample was pre-treated in a He stream at 100°C for 30 min prior to running the TPR experiment and then cooled to room

temperature in He. The TPR was carried out by ramping the sample to a temperature of 800°C in a reducing feed gas of 5% H_2 in argon at a flow rate of 1.1 Nml/s. The sample was cooled to room temperature and then subjected to TPO under 20% CO_2 in helium up to 800°C. During both TPR and TPO, the temperature was linearly ramped at a constant rate of 0.5°C/s. The H_2 and CO_2 consumption were monitored by OmniStar Pfeiffer mass spectrometer (MS) (OmniStar, Pfeiffer Vacuum). In addition, the stability of performance of the materials was tested through prolonged use of the material in isothermal redox cycling at 750°C using alternate H_2 reduction and CO_2 reoxidation, with intermediate He purging.

2.3. In situ X-Ray Diffraction (XRD) analysis

The crystallographic changes during H_2-TPR, CO_2-TPO and isothermal cycling were followed with in situ XRD in a home-built reaction chamber housed inside a Bruker-AXS D8 Discover apparatus (Cu Kα radiation of 0.154 nm). The reactor chamber was equipped with a Kapton foil window for X-ray transmission. A linear Vantec detector allowed covering a 2θ range of 20° with an angular resolution of 0.1°. For each sample, approximately 10 mg of powdered sample was evenly spread on a single crystal Si wafer. Interaction of the catalyst material with the Si wafer was never observed. Before each experiment, the reactor chamber was evacuated to a base pressure of 4 Pa by a rotation pump. Gases were supplied to the reactor chamber from a rig with calibrated mass-flow meters.

A full XRD scan (10° to 65° with a step of 0.02°) was performed at room temperature before and after each TPR, TPO and isothermal cycling experiment. The TPR was performed in flow conditions of 5%H_2/He at 1.1 Nml/s up to a temperature of 800°C. This was followed by reoxidation with 100% CO_2 at the same flow rate up to 800°C. Both of these treatments were performed at a uniform rate of 0.5°C/s to maintain similar conditions during the TPR and TPO in both the in situ XRD and the Micromeritics set up. The isothermal redox experiments were carried out at a temperature of 750°C with alternating H_2 reduction and CO_2 reoxidation sequences at a constant flow rate of 1.1 Nml/s each. As a means for testing stability of the oxygen carrier material, several samples were subjected to 5 subsequent redox cycles.

2.4. Experimental Reactor Setup

Test measurements were carried out at atmospheric pressure in a quartz tube microreactor (i.d. 10 mm), placed in an electric furnace. Typically, 30 mg of sample was packed between quartz wool plugs. The samples were diluted by quartz with a ratio of 1:10. The temperature of the catalyst bed was measured with K-type thermocouples touching the outside and inside of the reactor at the position of the catalyst bed. In all experiments, the material was reduced by 5% H_2/Ar and reoxidized by CO_2. The total flow rate of the feed gas into the reactor was maintained constant at 1.1 Nml/s by means of Brooks mass flow controllers. The performance of the samples was investigated at 750°C. The feed and product gas streams

were monitored online using an MS. The response of the mass spectrometer detector was regularly verified with calibration gases. A carbon balance with a maximum deviation of 15% was obtained.

Hydrogen consumption originates from reduction of Fe_2O_3 to Fe and of $MgFe^{3+}AlO_x$ to $MgFe^{2+}AlO_x$. In each cycle, reoxidation by CO_2 occurs for Fe and $MgFe^{2+}AlO_x$ to Fe_3O_4 and $MgFe^{3+}AlO_x$, respectively. The further oxidation of Fe_3O_4 to Fe_2O_3 can only be achieved by application of gaseous oxygen. Consumption of H_2 and CO_2 are connected in that these molecules respectively consume and provide one oxygen atom. Hence, the molar amount of hydrogen consumption during reduction corresponds with the molar amount of carbon monoxide production during CO_2 reoxidation. The CO yield was calculated from the ratio of the amount of CO produced and the total amount of Fe in the sample as in equation (1):

$$Y_{CO} = (n_{CO}(mol\ CO))/n_{Fe}(mol\ Fe)) \qquad (1)$$

Y_{CO} – CO Yield; n_{CO} –Amount of CO produced (mol);
n_{Fe} – Total amount of Fe (mol).
Experiments were repeated three times with as prepared sample material in order to obtain standard deviations. The standard error was found to be 10%.

3. Results
3.1. Material characterization

The XRD patterns of the as prepared oxygen storage materials are shown in Figure 1. The sharp diffraction lines observed in samples 100- to 50-Mg-Fe-Al-O were assigned to Fe_2O_3. With decreasing Fe_2O_3 content, new diffraction peaks appear and these intensify as the loading further decreases. Pure $MgAl_2O_4$ has diffractions situated at 31.3° (220), 36.9° (311), 44.8° (400), 59.4° (511) and 65.2° (440) mainly and its lattice parameter amounts to 8.083 Å (PDF: 021-1152). The presently observed diffractions, stemming from the Mg-Fe-Al-O promoter material, lie close to these angle values.
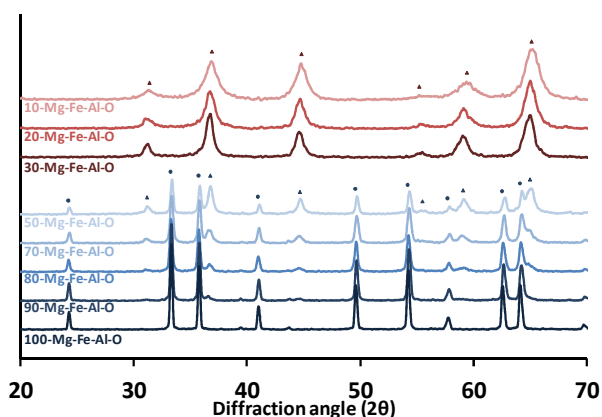

Fig.1. XRD spectra for as prepared X-Mg-Fe-Al-O samples, in various compositions (X = equivalent wt% of total amount of Fe_2O_3 in the sample); diffractions: (▲) $MgFeAlO_x$, (●) Fe_2O_3.
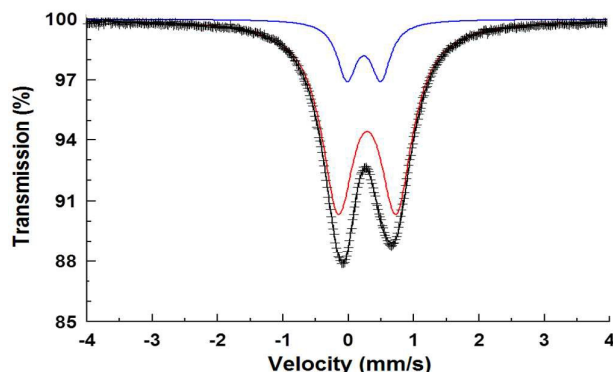
Fig.2. Mössbauer spectrum of 30-Mg-Fe-Al-O. The red and the blue deconvolutions represent two distinct Fe^{3+} doublets.

For all sample compositions, a lattice parameter of 8.101 Å was calculated, i.e. slightly higher than for pure $MgAl_2O_4$. This expansion in lattice can be explained by the substitution of Fe^{3+} for Al^{3+} in the spinel structure, as the Fe^{3+} cation (0.060nm) has a larger radius than Al^{3+} (0.053nm). For lower loadings of Fe_2O_3, peaks of Fe_2O_3 were no longer observed. This indicates that either Fe_2O_3 is finely dispersed or has been fully incorporated into the lattice of $MgAl_2O_4$. The Mössbauer spectrum for as prepared 30-Mg-Fe-Al-O revealed an asymmetric doublet structure (Figure 2)[41, 42]. It was adequately fitted by a superposition of two (symmetric) Lorentzian-shaped quadrupole doublets D1 (red component in Figure 2) and D2 (blue component in Figure 2) indicating at least two Fe sites. The obtained values for the isomer shift δ^{Fe} and the quadrupole splitting ΔE_Q clearly indicated that the Fe species in this sample are trivalent (Table 1).

Table 1. Mössbauer parameters for sample 30-Mg-Fe-Al-O, as prepared (Figure 2), after 4 min H_2 reduction (Figure 12a), after 4 min H_2 reduction and subsequent 4 min CO_2 reoxidation (Figure 12b), and after H_2-TPR to 900°C (Figure 13). D: doublet, δ^{Fe}: isomer shift, ΔE_Q: quadrupole splitting, Γ: line width (full width at half maximum), RA relative spectral area; S: sextet, $2\varepsilon_Q$: sextet quadrupole shift, H_{hf}: magnetic hyper fine field.

30-Mg-Fe-Al-O	Doublet/sextet	δ^{Fe} mm/s	$\Delta E_Q/2\varepsilon_Q$ mm/s	Γ mm/s	H_{hf} kOe	RA
As prepared	D1	0.40	0.89	0.61		0.84
	D2	0.35	0.52	0.36		0.16
H_2-reduced	D1	0.35	0.93	0.62		0.66
	D2	0.32	0.53	0.28		0.08
	D3	1.29	2.40	0.36		0.12
	D4	1.15	1.89	0.81		0.14
CO_2-reoxidized	D1+D2	0.37	0.82	0.66	-	0.56
	D3+D4	1.20	2.39	0.69	-	0.27
	S1	0.52	-0.04	-	387	0.10
	S2	0.31	0.04	-	239	0.07
H_2-reduced to 900°C	D1+D2	0.22	1.09	0.64	-	0.18
	D3+D4	1.21	2.39	0.57	-	0.20
	S1	0.108	0.004	-	339	0.62

They could be ascribed to Fe^{3+} partly in tetrahedral (A) and partly in octahedral (B) lattice sites, respectively. On the other

hand, considering the broad line width Γ of the dominant doublet D1, the observed asymmetric line shape might actually be explained by the presence of a more or less broad distribution of δ^{Fe} and ΔE_Q values, possibly due to non-uniform distortions of the site symmetries as a result of unordered cation distribution. The absence of a sextet signal indicated that Fe was not present as Fe_2O_3, which is in line with the XRD pattern of 30-Mg-Fe-Al-O, where no diffractions of Fe_2O_3 show. Hence, for samples with low Fe_2O_3 loading, all Fe was incorporated as Fe^{3+} into the spinel structure in at least 2 different sites. Based on XRD and Mössbauer, this spinel phase can thus be written as Mg-Fe-Al-O.

The crystallite sizes of all as prepared samples were calculated using the Scherrer equation. The iron oxide crystallite sizes decreased from 139 to 60nm with decreasing loading from 100 to 50wt% Fe_2O_3 (Figure 3a). In general the $MgFeAlO_x$ phase exhibited smaller crystallite sizes (10-22nm) when compared to those of Fe_2O_3 (Figure 3a). The results of the N_2-B.E.T. analysis showed an increase in surface area with decreasing Fe_2O_3 content (Figure 3b).
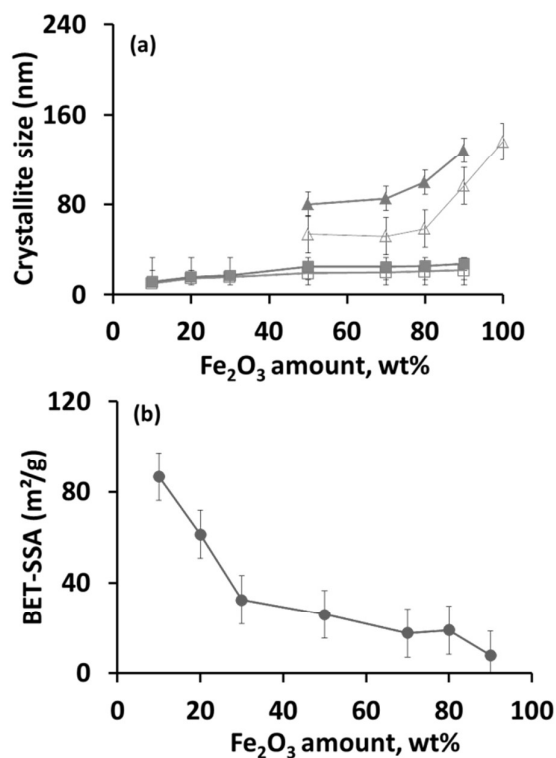

Fig.3. Crystallite size and BET surface area as function of Fe_2O_3 amount in the sample. (a) Crystallite size of Fe_2O_3 and Mg-Fe-Al-O phases in the samples. As prepared: (□) $MgFeAlO_x$ and ( ) Fe_2O_3; (■) $MgFeAlO_x$ and ( ) Fe_3O_4 after 5 isothermally redox cycles at 750°C. Crystallite size calculated based on XRD data using the Scherrer equation. (b) B.E.T. specific surface area for as prepared samples. The error bar indicates the standard deviation.
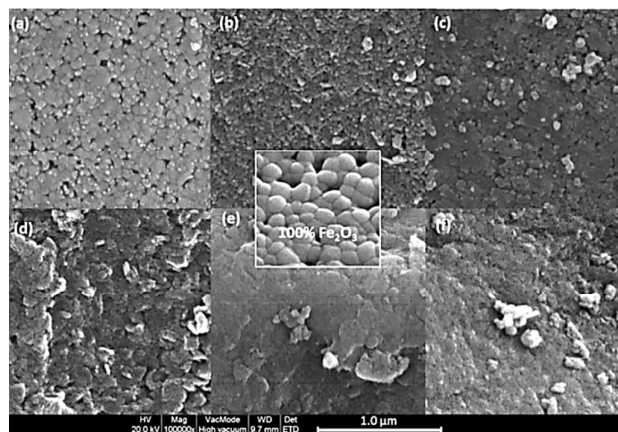
Fig.4. SEM images of various as prepared samples: (a) 90-Mg-Fe-Al-O, (b) 70-Mg-Fe-Al-O, (c) 50-Mg-Fe-Al-O, (d) 30-Mg-Fe-Al-O, (e) 20-Mg-Fe-Al-O, (f) 10-Mg-Fe-Al-O; central inset: Fe_2O_3.

The SEM images of various Mg-Fe-Al-O materials are shown in Figure 4. For 90-Mg-Fe-Al-O large and small particles appeared. Based on the XRD pattern, the larger particles correspond to Fe_2O_3, while the fine ones pertain to $MgFeAlO_x$ spinel. The crystallite sizes tended to decrease quite significantly between 90- and 50-Mg-Fe-Al-O when compared to pure Fe_2O_3 (Figure 4a-c, inset). Samples with Fe_2O_3 loadings below 50wt% exhibited a much smaller spinel crystallite size, see Figure 4(d-f).

3.2. Reactivity and stability tests

The results of CO yield with respect to the iron content are shown in Figure 5. The initial CO yield lies between 0.5 and 0.7 mol_{CO}/mol_{Fe} for all samples, with highest value for 70- and 10-Mg-Fe-Al-O. After 10 cycles, 10-Mg-Fe-Al-O shows the highest CO yield (0.65 mol_{CO}/mol_{Fe}), which is only slightly below its initial value. This yield lies below the theoretical value, which amounts to 1.33 mol_{CO}/mol_{Fe}. Mg-Fe-Al-O materials with Fe_2O_3 loading between 20 and 50wt% show a similar CO yield (0.45 to 0.5 mol CO/mol Fe). When the Fe_2O_3 content is higher, the CO yield quickly decays. No side product in the form of carbon was observed. For comparison, the same redox activity and stability experiment has been performed on 10 Fe_2O_3-Al_2O_3 and 10 Fe_2O_3-MgO, with the same amount of Fe_2O_3 as 10-Mg-Fe-Al-O. Both reference materials present a 10 fold lower CO yield after 10 cycles than 10-Mg-Fe-Al-O, proving the beneficial action of the Fe-modified spinel. Moreover, also the most active compositions in these materials, namely 50wt%Fe_2O_3-Al_2O_3 and 50wt%Fe_2O_3-MgO, showed low stability and three times lower activity than our best 10-Mg-Fe-Al-O material.

The CO yield per mole Fe for the Mg-Fe-Al-O materials after 10 cycles almost follows the inverse order of Fe_2O_3 loading, with 50-Mg-Fe-Al-O slightly out of line. The order of the CO yield thus aligns with the decrease in Fe_2O_3 XRD intensity (Figure 1) as well as the decreasing Fe_2O_3 particle size as indicated for the Fe_2O_3 loadings in Figure 3a. Based on XRD

and Mössbauer, samples containing lowest loadings of Fe_2O_3 (≤30wt%) have all of the iron oxide incorporated into the spinel phase. This phenomenon leads to a high CO yield per mole of Fe and also less deactivation.
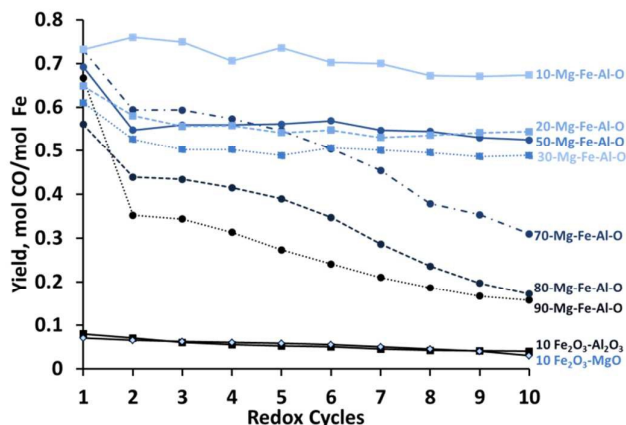

Fig.5. CO yield in redox cycles for the series of X-Mg-Fe-Al-O samples and for two reference materials 10 Fe_2O_3-Al_2O_3 and 10 Fe_2O_3-MgO. Each cycle (16 min) is composed of 4 min H_2 (5% in Ar), 4 min He, 4 min CO_2 and 4 min at 750ºC. All the gas flows were 1.1 Nml/s.

To study the effect of sintering on Mg-Fe-Al-O materials with lower Fe_2O_3 loadings (≤50wt%), prolonged cycling was performed. The CO yield per mole Fe of 25 redox cycles using 50-Mg-Fe-Al-O as oxygen carrier material is depicted in Figure 6. A very high CO production was observed during the initial cycle. However, upon cycling continued deactivation does occur and the final yield is less than half of the original value.
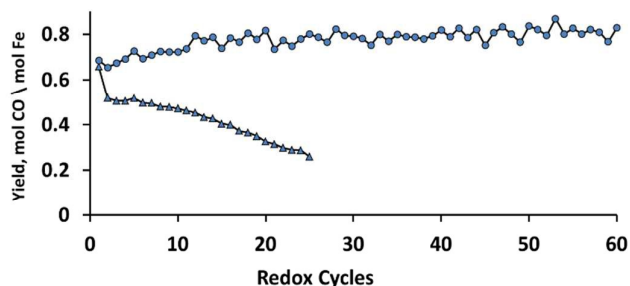

Fig.6. CO yield as a function of number of isothermal redox cycles for oxygen carrier materials ( ) 10-Mg-Fe-Al-O and (▲) 50-Mg-Fe-Al-O. Each cycle (16 min) is composed of 4 min H_2 (5% in Ar), 4 min He, 4 min CO_2 (100%) and 4 min He at 750ºC. All the gas flows were 1.1 Nml/s.

Figure 6 also shows the results of 60 isothermal redox cycles using 10-Mg-Fe-Al-O as oxygen carrier material. With respect to the yield of CO, despite some fluctuations, the results are quite stable. Hence, from the previous yield and stability measurements, it is concluded that the content of Fe_2O_3 should definitely be lower than 50wt% to obtain structural stability.

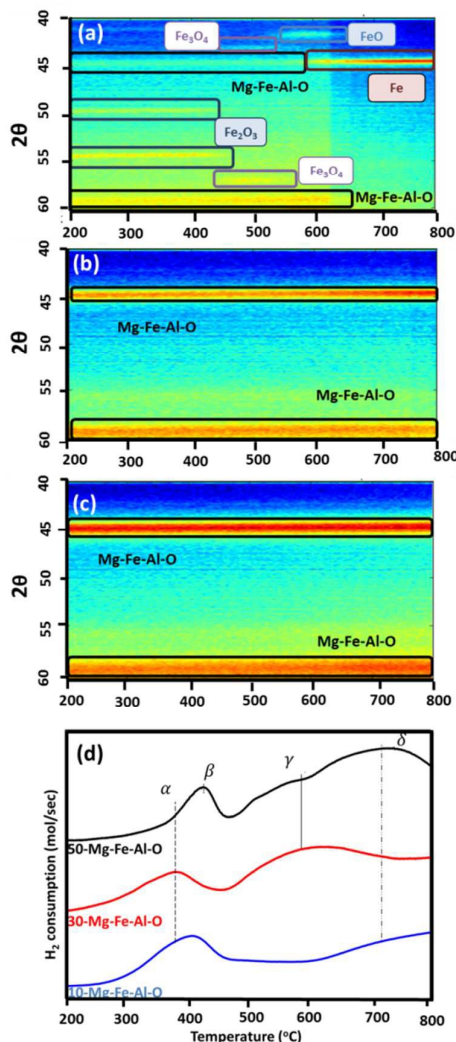10-Mg-Fe-Al-O remains stable for 60 cycles under operating conditions.

Fig.7. In situ XRD pattern recorded during H_2-TPR for (a) 50-Mg-Fe-Al-O, (b) 30-Mg-Fe-Al-O, (c) 10-Mg-Fe-Al-O; (d) Conventional H_2-TPR for 50-, 30- and 10-Mg-Fe-Al-O. The samples were heated from room temperature to 800°C with heating rate 0.5°C/s. Gas flow: 1.1 Nml/s H_2 (5 % in Ar).

3.3. In situ XRD

The changes in the crystal structure for all modified iron oxide materials were monitored by in situ XRD measurements during H_2-TPR, CO_2-TPO and isothermal redox cycling.

3.3.1. H_2-TPR

Figure 7 displays the time-resolved in situ XRD during H_2-TPR of samples 50-, 30- and 10-Mg-Fe-Al-O, along with the H_2-TPR consumption profile of these materials in a conventional TPR reactor. 50-Mg-Fe-Al-O (Figure 7a) shows reduction of hematite (isolated angles 2θ at 41°, 50°, 54°) to magnetite (2θ at 43°, 57°) at 450°C and reduction of magnetite to wuestite

(2θ=42°) at 550°C. The transition of FeO to metallic Fe (2θ=45°) starts at a temperature of 600°C. In addition, diffraction peaks are present from the spinel phase $MgFeAlO_x$, at 45° overlapping with the Fe diffraction and at 59°, up to the temperature of 800°C. For 30-Mg-Fe-Al-O only characteristic diffractions from the $MgFeAlO_x$ spinel are observed throughout the whole temperature range (Figure 7b).

However, the intensity of the 45° diffraction is seen to increase from ~600°C onward. The latter could indicate the presence of an additional diffraction originating from Fe metal, which has segregated from the spinel phase during reduction. For sample 10-Mg-Fe-Al-O, Figure 7c, only spinel diffractions appear throughout the entire temperature range. Hence, the spinel material is not noticeably reduced in this temperature window.

The reduction of these materials was examined further through conventional H_2-TPR experiments. Figure 7d represents reduction profiles of the 50-, 30- and 10-Mg-Fe-Al-O samples. For 50-Mg-Fe-Al-O, the first maximum of hydrogen consumption is at β~440°C. Based on Figure 7a, this corresponds to the transformation of hematite to magnetite. Further reduction of hematite to wuestite starts at 500°C, with a local maximum around 580°C, which is however overlapping with the onset of reduction to metallic Fe yielding an asymmetric transition to the maximum of FeO - Fe reduction at δ ~740°C. This profile was typical in all materials with loadings higher than 50wt% Fe_2O_3. For low loadings of Fe_2O_3 (≤30wt%), the first reduction peak α lies at ~400°C, followed by a broad maximum at 600°C for 30-Mg-Fe-Al-O or above 800°C for 10-Mg-Fe-Al-O. In the case of 30-Mg-Fe-Al-O, the second maximum could correspond to reduction and segregation of Fe from the spinel structure, as the intensity change in the XRD pattern suggests. For 10-Mg-Fe-Al-O on the other hand, XRD gives no additional information as no structural transitions appear. Hence, it must be concluded that reduction occurs through loss of oxygen without major restructuring of the material. Rather, subtle transitions between different spinel types may occur, which go unnoticed in XRD as their diffractions lie too close to be distinguished.

3.3.2. CO_2-TPO

The H_2-TPR was immediately followed by a CO_2-TPO. The 2D maps for in situ XRD of these same samples are shown in Figure 8 along with the conventional reoxidation profiles. During oxidation of 50-Mg-Fe-Al-O (Figure 8a), Fe is present up to 550°C and then reoxidizes into magnetite. Weak spinel lines are visible throughout the TPO. A wuestite pattern was not observed. This suggests that wuestite either occurs as highly reactive intermediate between metallic iron and magnetite, or it is not formed at all under the present conditions.

The reoxidation of 30-Mg-Fe-Al-O (Figure 8b) starts off with a strong 45° diffraction, representing the superposition of the spinel and Fe metal diffraction. Oxidation of metallic iron to magnetite (2θ=57°) combined with the spinel signal results in a broad signal between 2θ=56°-59°. Around 500°C, a clear intensity change occurs at 2θ =44°-45°. This relates to the

disappearance of the Fe metal diffraction contribution at 45°. Just like in H_2-TPR, 10-Mg-Fe-Al-O (Figure 8c) shows only 2 diffraction lines without significant intensity variation.
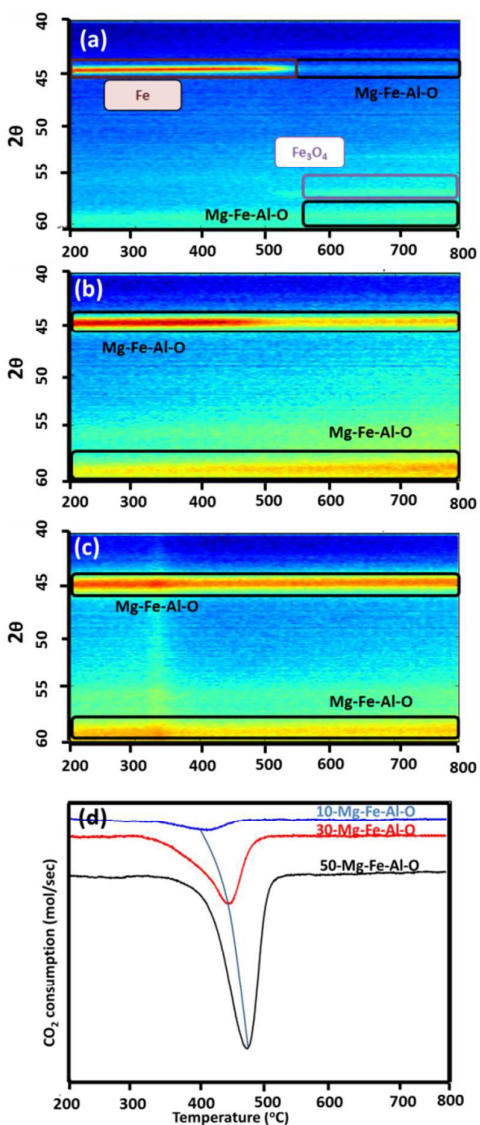

Fig.8. In situ XRD pattern during CO_2-TPO for (a) 50-Mg-Fe-Al-O, (b) 30-Mg-Fe-Al-O and (c) 10-Mg-Fe-Al-O; (d) Conventional CO_2-TPO for Mg-Fe-Al-O promoted iron oxides. The samples were heated from room temperature to 800°C with heating rate 0.5°C/s. Gas flow: 1.1 Nml/s CO_2

Conventional CO_2-TPO experiments following the H_2-TPR, are presented in Figure 8d. After reduction of pure hematite to metallic iron, oxidation appears to occur in one step. As seen in Figure 8a wuestite is not observed as intermediate and a single-step oxidation from metallic iron to magnetite is observed in 50-Mg-Fe-Al-O and higher loadings (not shown). 30-Mg-Fe-Al-O and 10-Mg-Fe-Al-O also show a TPO signal that corresponds to a single step oxidation at ~450°C and ~420°C as indicated in Figure 8d. With increasing promoter content, the general trend is that reoxidation by CO_2 occurs at lower temperature due to stabilization of the spinel particle size.

The in situ TPR and TPO investigations showed various phases of iron oxides for materials with Fe_2O_3 loadings higher than 50wt%. For lower loadings the spinel was the predominant phase and the formation of other phases was difficult to discern due to close overlap of peaks of iron oxides and spinel. Hence, a higher temperature TPR and TPO was performed to study the reducibility of the material to metallic Fe. The high temperature in situ H_2 reduction study up to 900°C for 30-Mg-Fe-Al-O is represented in Figure 9a. It shows close overlap of the diffraction patterns of spinel $MgFeAlO_x$ and metallic Fe. This makes it difficult to distinguish the appearance of the Fe phase explicitly from the in situ XRD pattern during reduction. But the formation of metallic Fe could be discerned from the ex situ XRD diffraction peaks in Figure 9b. Despite the close overlap between spinel and metallic Fe diffractions, the presence of metallic Fe could be deduced from the relative intensity of the less intense spinel peak (400) at $2\theta=45°$, which is higher than its most intense peak (311) at $2\theta=36°$. The increase in intensity of the peak at $2\theta=45°$ and the shoulder at $2\theta=65°$, matching with the characteristic diffractions of metallic Fe, clearly indicate Fe formation.
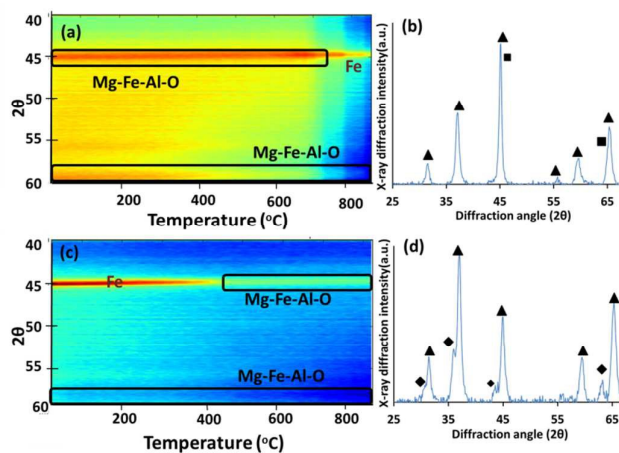

Fig.9. (a) In situ XRD pattern of 30-Mg-Fe-Al-O during H_2-TPR between room temperature and 900°C and (b) XRD full scan of 30-Mg-Fe-Al-O at room temperature after H_2 reduction. (c) In situ XRD pattern of 30-Mg-Fe-Al-O during CO_2-TPO between room temperature and 900°C and (d) full range scan after the reoxidation of 30-Mg-Fe-Al-O at room temperature. (▲) Mg-Fe-Al-O, ( ) Fe and ( ) Fe_3O_4; Gas flows: 1.1 Nml/s H_2 (5% in Ar) and 1.1 Nml/s CO_2. Heating rate: 0.5°C/s.

The lattice parameter calculation of the XRD post TPR shows that the spinel lattice parameter is 8.101 Å, indicating the spinel $MgFeAlO_x$ with incorporated Fe remains stable even at these temperatures. This indicates that only partial segregation of Fe from the spinel occurs at 900°C and even higher temperatures are required for further decomposition of the spinel.

Figure 9c shows the in situ CO_2-TPO reoxidation of Fe and spinel, where no clear diffractions from Fe_3O_4 were observed. The full scan in Figure 9d shows that Fe_3O_4 is indeed present as

indicated by its characteristic diffraction peaks. The post- TPR and TPO patterns thus show that part of the iron oxide in the spinel can be reduced to metallic Fe and then back to Fe_3O_4, while the overall spinel structure remains stable even at $900^\circ C$.

3.3.3. Isothermal redox cycles

As a means for identifying the structural changes in the oxygen carrier material during reaction, two samples were subjected to 5 subsequent redox cycles, while being monitored in situ with XRD: 50-Mg-Fe-Al-O and 10-Mg-Fe-Al-O as the latter presents the highest CO yield and stability. The results of the in situ XRD for 50-Mg-Fe-Al-O during five isothermal redox cycles at $750^\circ C$ are shown in Figure 10a. As cycling proceeds, the reduction of magnetite ($2\theta=57^\circ$) to metallic Fe ($2\theta=45^\circ$) becomes incomplete and a mixture of FeO ($2\theta=42^\circ$) and Fe is observed after each half-cycle. The residual signal around $2\theta=45^\circ$, observed in oxidation steps, as well as the diffraction peak at $2\theta=59^\circ$ are characteristic for $MgFeAlO_x$ spinel.
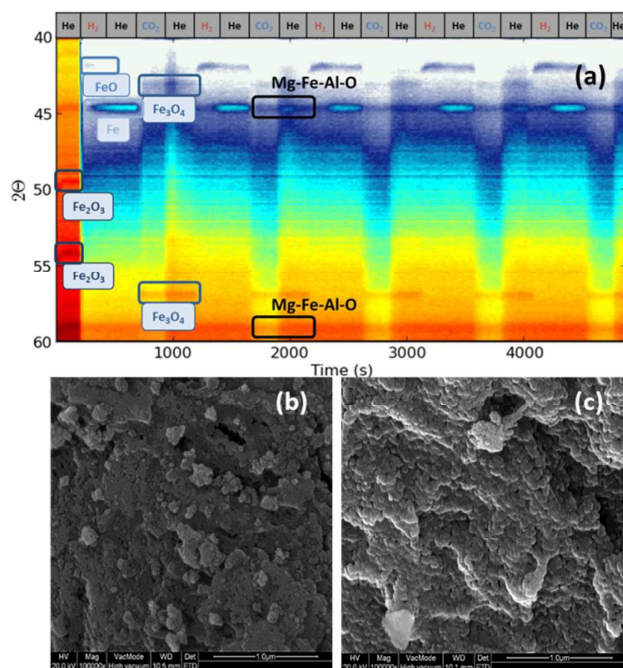
chemical looping conditions (Figure 11a). Thus, the spinel contributes towards stability and provides fine dispersion of Fe in the material which could be the reason for its high CO yield. SEM images of the as prepared sample (Figure 11b) and spent sample, after 60 isothermal redox cycles (Figure 11c), also show one type of material. The material morphology in as prepared and spent sample is quite similar, indicative of a spinel stable in redox cycling. Figure 3 shows the changes in crystallite size in all samples after isothermal cycles. The average crystallite sizes calculated from SEM are in agreement with the values calculated from XRD. The $MgFeAlO_x$ phase shows a quite stable crystallite size when compared to its as prepared values. When iron oxide is present as a separate phase, it does suffer from sintering, with a stronger increase in size as a consequence.
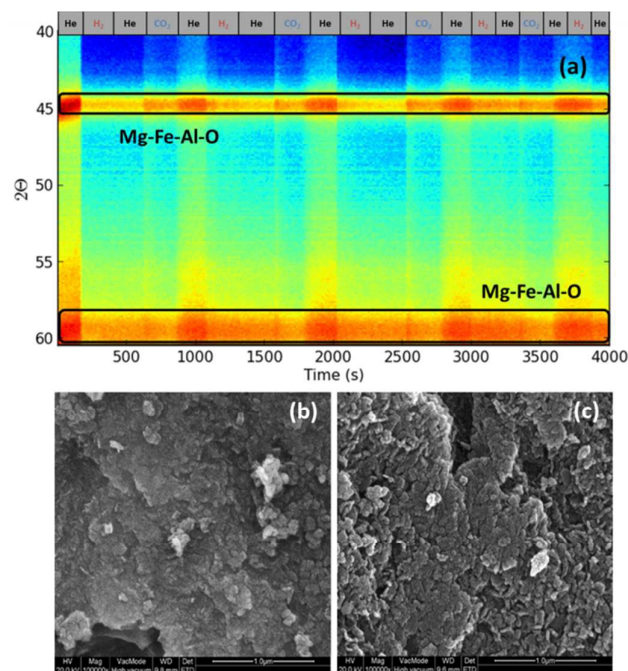

Fig.10 (a) In situ XRD during five isothermal redox cycles at $750^\circ C$ for 50-Mg-Fe-Al-O. SEM micrographs of the (b) as prepared material and (c) after 5 cycles. Each cycle (16 min) comprises alternate pulses of 4 min H_2 (5% in Ar), 4 min He, 4 min CO_2 and 4 min He. All gas flows were 1.1 Nml/s.

The SEM image of the as prepared 50-Mg-Fe-Al-O sample in Figure 10b shows only one type of morphology with a particle size ~37nm. The presence of two different phases of Fe_2O_3 and $MgFeAlO_x$ was however confirmed by XRD as shown in Figure 1. The SEM image of the sample after five times redox cycling in Figure 10c shows an increase in crystallite size to ~59nm due to sintering. The presence of two different morphologies was again identified only using XRD.

For 10-Mg-Fe-Al-O, the in situ XRD measurements during cycling show that the $MgFeAlO_x$ phase remains stable in

Fig.11 (a) In situ XRD for five isothermal redox cycles at $750^\circ C$ for 10-Mg-Fe-Al-O. SEM micrographs of the 10-Mg-Fe-Al-O (b) as prepared and (c) after 60 isothermal redox cycles at $750^\circ C$. Each cycle (16 min) comprises alternate pulses of 4 min H_2 (5% in Ar), 4 min He, 4 min CO_2 and 4 min He. All the gas flows were 1.1 Nml/s.

3.4. Mössbauer analysis

The Mössbauer analysis of the 30-Mg-Fe-Al-O sample after a single reduction half-cycle and after subsequent reoxidation are shown in Figure 12a and b.

The spectrum of the sample after H_2 reduction revealed the presence of four quadrupole doublets as shown in Figure 12a. The subspectra D3 and D4 were irrefutably assigned to Fe^{2+} species, D1 and D2 to Fe^{3+}. These results showed that the two different Fe sites were both affected by reduction.
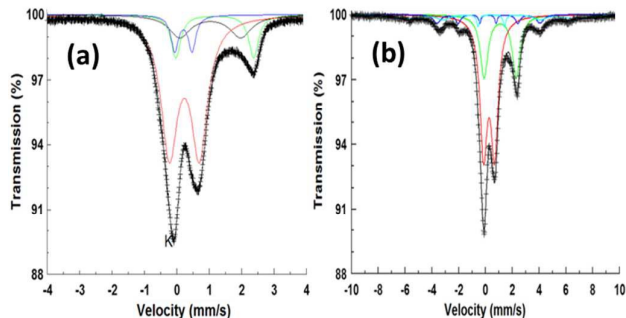
Fig.12: Mössbauer spectra of 30-Mg-Fe-Al-O after isothermal (a) H_2 reduction (b) CO_2 reoxidation. Red (D1) and blue (D2): Fe^{3+} doublets; Green (D3) and black (D4): Fe^{2+} doublets.

Further, the doublets D1 (Fe^{3+}) and D4 (Fe^{2+}) concerned the same Fe site, and so did D2 (Fe^{3+}) and D3 (Fe^{2+}). The Fe^{2+}/Fe^{3+} ratio for this sample was estimated to be 0.37 ± 0.03, hence not all iron oxide species in 30-Mg-Fe-Al-O were reduced in the 4 min H_2 exposure.

The fit results are shown in Table 1. In contrast to the H_2-TPR experiment followed with in situ XRD on this same sample, Mössbauer analysis found no evidence for the presence of Fe. This is related to the fact that only 4 minutes of reduction were applied to the sample before performing the Mössbauer measurement, while in TPR, the sample undergoes a more extended reduction.

The reoxidized spectrum in Figure 12b still revealed the same doublets, indicating that the majority of the Fe species remained in the spinel phase. In addition to these doublets, the appearance of two weak sextet components, S1 and S2, was recognized, pointing towards the presence of magnetic Fe phases. In view of the extended velocity scale and hence lower resolution, the two ferric and ferrous doublets of the spinel contribution were less resolved and hence fitted using only one Fe^{3+} doublet, covering the previous D1 and D2, and one Fe^{2+} doublet (D3+D4). The fit results are tabulated in Table 1. The parameter values of the composed Fe^{3+} and Fe^{2+} doublet subspectra, denoted (D1+D2) and (D3+D4) in Table 1, were in line with the average values of the parameters of the separated doublets D1 and D2, and D3 and D4, respectively, as resolved from the previous spectra (Table 1). This implies that a major fraction of the 30-Mg-Fe-Al-O spinel phase was not drastically affected by the subsequent treatments. Based on the δ^{Fe} values of the sextets, these could arise from some magnetically ordered Fe^{3+} oxide(s), segregated from the spinel structure, but their specific origin remains uncertain.

In order to enhance the effect of reduction upon 30-Mg-Fe-Al-O as observed in the Mössbauer spectrum of Figure 12, a more deep reduction was pursued with this material by exposure to H_2-TPR up to 900°C. The corresponding Mössbauer spectrum is displayed in Figure 13. It consists of a central contribution containing a Fe^{3+} and Fe^{2+} doublet, as well as a sharp sextet component.
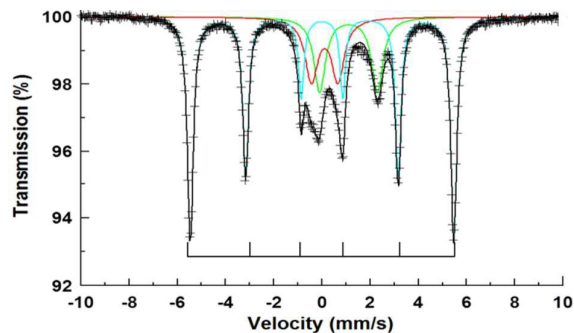

Fig.13. Mössbauer Spectra of 30-Mg-Fe-Al-O after H_2-TPR at 900°C. Red: Fe^{3+} doublet. Green: Fe^{2+} doublet. Cyan and inset line markers: α-Fe sextet.

The hyperfine parameters of the sextet were characteristic for metallic Fe, α-Fe (Table 1). This indicates the formation of metallic Fe as previously deduced from the full XRD scans after high temperature H_2-TPR. Further, it also shows the existence of Fe^{3+} and Fe^{2+} ions even after reduction at 900°C, confirming that the $MgFeAlO_x$ spinel is stable even at these high temperatures and that complete decomposition of the spinel is not achieved.

4. Discussion

The present study using in situ XRD, Mössbauer and prolonged cycling tests addresses three most important aspects of a chemical looping process, i.e. (i) stability, (ii) product yield and (iii) optimum oxygen storage capacity. Stability of the materials is an indicator of the material's resistance to sintering. It is well known that pure Fe_2O_3 deactivates rapidly due to sintering. Sintering is essentially a process, limited by diffusion of metal cations [26, 43-45], which leads to agglomeration of iron particles, without however changing the total oxygen storage capacity. This phenomenon leads to increase in particle size and a decline in overall surface area. The latter entails a decline in product yield, as surface area and redox activity play a complementary role during the reaction[46-48]. Hence, it is crucial to eliminate the contact between adjacent iron oxide particles.

Previous studies show that addition of materials like CeO_2, ZrO_2, $CeZrO_2$, La_2O_3, MgO and Al_2O_3 prevent sintering by acting as a physical barrier between adjacent iron oxide particles[26, 49-53]. The interaction of the aforementioned materials with iron oxides may lead to formation of various structures like $CeFeO_3$, $LaFeO_3$, $MgFe_2O_4$ and $FeAl_2O_4$[26, 49-53]. However, the formation of these structures results in a decrease in the amount of oxygen available for reaction. This lower oxygen storage capacity leads to a decrease in product yield. These materials also require a high temperature for reduction and oxidation, leading to higher operating temperatures.

In the present study, the incorporation of Fe in a spinel $MgFeAlO_x$ leads to enhanced stability and CO yield of the materials. Small amounts of iron are fully incorporated into the spinel structure, while for larger loadings, a separate Fe_2O_3 phase is formed. Hence, the materials synthesized can be written as either $MgFeAlO_x$ or $Fe_2O_3/MgFeAlO_x$. Spinel

particles have smaller as prepared sizes than Fe_2O_3. Highest stability in this study is obtained for materials with predominant $MgFeAlO_x$ phase i.e. without Fe_2O_3 phase separation. In prolonged cycling at 750°C, 10-Mg-Fe-Al-O remains particularly stable.
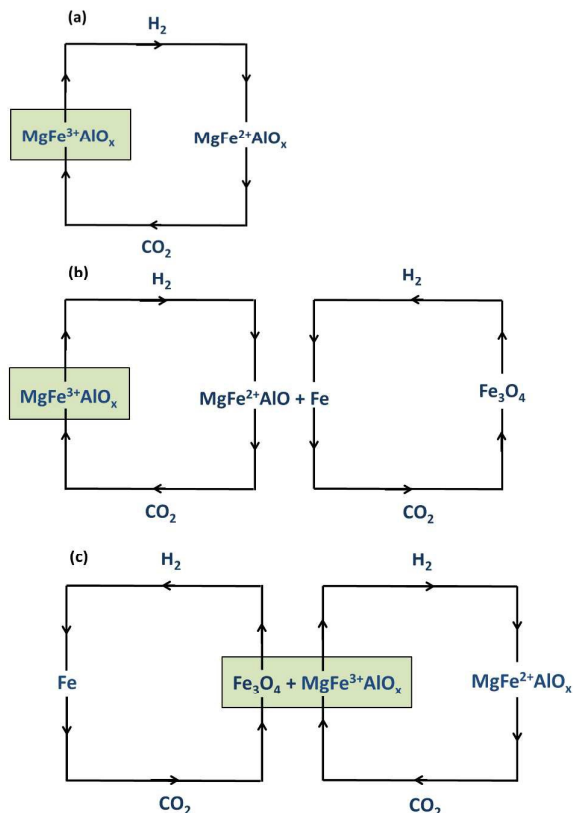

Fig.14: Reduction and oxidation pathways of various oxygen carrier materials: (a) $MgFeAlO_x$ spinel phase at temperature < 750°C, (b) spinel phase at temperature > 750°C, (c) mixed $Fe_2O_3/MgFeAlO_x$ phase.

All spinel structures without separate iron oxide phase are stable at high temperature as seen from the isothermal cycles at 750°C. In addition and unlike the other spinel forms studied before, they exhibit a lower reduction and reoxidation temperature in conventional H_2-TPR and CO_2-TPO profiles. The spinel phase can be reduced and reoxidized back to $MgFe^{3+}AlO_x$ without the formation of any intermediate structures. Based on in situ XRD and Mössbauer, the spinel reduction can be described as $MgFe^{3+}AlO_x \rightarrow MgFe^{2+}AlO_x$ at temperatures lower than 750°C (Figure 14a), while segregation and reduction to metallic Fe is obvious for prolonged reduction or at higher temperatures according to $MgFe^{3+}AlO_x \rightarrow MgFe^{2+}AlO_x + Fe$ (Figure 14b). This ease in reduction and oxidation contributes to the increased CO yield of the spinel. The occurrence of a separate iron oxide phase, as for Fe_2O_3 loadings above 30wt% (Figure 14c), is always detrimental to the CO yield as it leads to enhanced sintering. While the $MgFeAlO_x$ spinel phase will always follow the redox scheme of

Figure 14a or b depending on temperature, the separate iron oxide phase will be reduced to Fe, but at the same time suffer from severe sintering. Indeed, the $MgFeAlO_x$ spinel suffers less from sintering based on particle size determination before and after cycling (Figure 3). Stabilization of Fe inside the spinel structure greatly improves the stability of the material in cycling.

The oxygen storage capacities of the materials were calculated and represented in Figure 15. For the materials 10- to 30-Mg-Fe-Al-O the cycling proceeds between Fe^{3+} and Fe^{2+}. For the materials with higher loadings of Fe_2O_3, the cycling in $Fe_2O_3/MgFeAlO_x$ will change the Fe oxidation state from Fe^{3+} and Fe^{2+} and back in spinel and between Fe^{3+} and Fe^0 in iron oxides. The current results for Mg-Fe-Al-O prove that oxygen storage capacity alone is not enough to make a good cycling material. Rather, reducibility (Figure 7) and stability (Figure 5) are of equal if not higher importance because they ensure durability. Hence, although the oxygen storage capacity of 10-Mg-Fe-Al-O is lowest of all materials because of its low Fe content, it proves to be the most stable and durable. This is ascribed to the redox properties combined with the structural stability, which are both equally important characteristics for oxygen carrier selection in chemical looping. These structural features make $MgFeAlO_x$ a promising candidate even though it has a much lower oxygen storage capacity when compared to $Fe_2O_3/MgFeAlO_x$ materials.
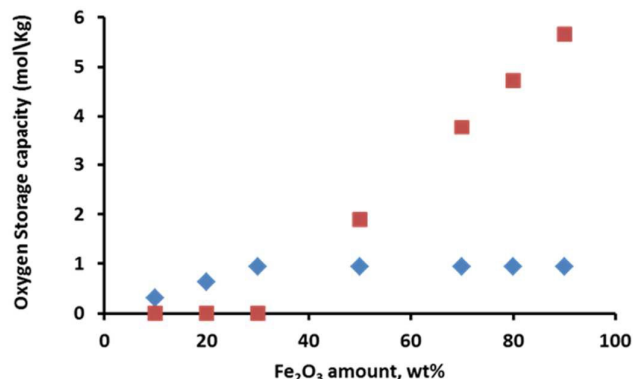

Fig. 15 Oxygen storage capacities of the materials from 10- to 90-Mg-Fe-Al-O. Oxygen storage capacities of ( ) separate Fe_2O_3 and (◆) iron incorporated in spinel.

Conclusions

A series of Mg-Fe-Al-O samples are prepared as oxygen storage materials for chemical looping processes in order to investigate the stability and CO yield. XRD and Mössbauer spectra of the as prepared materials confirm the formation of a spinel $MgFeAlO_x$ as crystallographic phase in all samples. An additional Fe_2O_3 phase is observed in samples with Fe_2O_3 loadings >30wt%. For decreasing content of Fe_2O_3, smaller crystallite sizes are obtained and for lowest Fe_2O_3 loadings, only a mixed $MgFeAlO_x$ spinel phase is observed.

For Fe_2O_3 loadings above 30wt%, redox cycling leads repeatedly to reduction from Fe_2O_3 to Fe_3O_4, FeO and Fe, while the spinel is only partially reduced. Nevertheless, samples with high Fe_2O_3 loading suffer from rapid deactivation during the first 10 cycles, due to sintering of the iron oxides. At lower loadings ($\leq$30wt%) most of the iron is in the form of $MgFeAlO_x$ which reduces and oxidizes back between Fe^{3+} and Fe^{2+}, leading to stable performance over prolonged period of time. This typical pattern is observed in the temperature range up to $750^{\circ}C$, while at higher temperature extraction of Fe from the spinel occurs due to high temperature reduction and segregation. Reoxidation of the segregated metallic Fe to Fe_3O_4 is confirmed by full XRD scans.

The $MgFeAlO_x$ spinel formation leads to highest efficiency of Fe for CO_2 utilization. Even though Fe incorporated inside the spinel has a low oxygen storage capacity when compared to $Fe_2O_3/MgFeAlO_x$, the stabilization of Fe in the form of $MgFeAlO_x$ results in improved performance. The best performing sample was 10-Mg-Fe-Al-O, showing only a spinel phase. Compared to 10wt% Fe_2O_3 supported on Al_2O_3 or MgO, the CO yield of this 10-Mg-Fe-Al-O spinel proves to be ten times higher. The spinel structure remained stable in isothermal cycling at 750°C and could retain this stability for over 60 cycles by partial cycling of Fe between Fe^{3+} to Fe^{2+}. Although the 10-Mg-Fe-Al-O spinel exhibits a low oxygen storage capacity, it can exchange this oxygen for a much longer time because it hardly changes in structure or particle size.

Acknowledgements

Notes and references

1. A. Levasseur, P. Lesage, M. Margni, L. Deschenes and R. Samson, *Environ Sci Technol*, 2010, **44**, 3169-3174.
2. J. G. Canadell, C. Le Quere, M. R. Raupach, C. B. Field, E. T. Buitenhuis, P. Ciais, T. J. Conway, N. P. Gillett, R. A. Houghton and G. Marland, *Proceedings of the National Academy of Sciences of the United States of America*, 2007, **104**, 18866-18870.
3. E. Zedillo, *Global Warming: Looking Beyond Kyoto*, 2008, 1-10.
4. L. S. Fan, L. Zeng, W. L. Wang and S. W. Luo, *Energ Environ Sci*, 2012, **5**, 7254-7280.
5. W. K. Jozwiak, E. Kaczmarek, T. P. Maniecki, W. Ignaczak and W. Maniukiewicz, *Applied Catalysis A: General*, 2007, **326**, 17-27.
6. S. Bhavsar, M. Najera and G. Veser, *Chemical Engineering & Technology*, 2012, **35**, 1281-1290.
7. P. C. Chiu and Y. Ku, *Aerosol Air Qual Res*, 2012, **12**, 1421-1432.
8. V. V. Galvita, H. Poelman, C. Detavernier and G. B. Marin, *Applied Catalysis B: Environmental*, 2015, **164**, 184-191.
9. Q. L. Song, W. Liu, C. D. Bohn, R. N. Harper, E. Sivaniah, S. A. Scott and J. S. Dennis, *Energ Environ Sci*, 2013, **6**, 288-298.
10. J. E. Readman, A. Olafsen, Y. Larring and R. Blom, *J Mater Chem*, 2005, **15**, 1931-1937.
11. C. L. Muhich, B. W. Evanko, K. C. Weston, P. Lichty, X. Liang, J. Martinek, C. B. Musgrave and A. W. Weimer, *Science*, 2013, **341**, 540-542.
12. V. V. Galvita, H. Poelman and G. B. Marin, *Topics in Catalysis*, 2011, **54**, 907-913.
13. V. V. Galvita, H. Poelman, V. Bliznuk, C. Detavernier and G. B. Marin, *Industrial & Engineering Chemistry Research*, 2013, **52**, 8416-8426.
14. V. V. Galvita, H. Poelman and G. B. Marin, *Journal of Power Sources*, 2015, **286**, 362-370.
15. M. Najera, R. Solunke, T. Gardner and G. Veser, *Chemical Engineering Research and Design*, 2011, **89**, 1533-1543.
16. A. Abad, J. Adanez, F. Garcia-Labiano, L. F. de Diego, P. Gayan and J. Celaya, *Chemical Engineering Science*, 2007, **62**, 533-549.
17. P. Cho, T. Mattisson and A. Lyngfelt, *Fuel*, 2004, **83**, 1215-1225.
18. V. Galvita, M. Filez, H. Poelman, V. Bliznuk and G. Marin, *Catalysis Letters*, 2014, **144**, 32-43.
19. J. Adanez, A. Abad, F. Garcia-Labiano, P. Gayan and L. F. de Diego, *Progress in Energy and Combustion Science*, 2012, **38**, 215-282.
20. T. Mattisson, A. Jardnas and A. Lyngfelt, *Energy & Fuels*, 2003, **17**, 643-651.
21. Q. Zafar, T. Mattisson and B. Gevert, *Energy & Fuels*, 2006, **20**, 34-44.
22. D. D. Miller and R. Siriwardane, *Energy & Fuels*, 2013, **27**, 4087-4096.
23. V. Galvita, T. Schroder, B. Munder and K. Sundmacher, *Int J Hydrogen Energ*, 2008, **33**, 1354-1360.
24. M. Tang, L. Xu and M. Fan, *Applied Energy*, 2015, **151**, 143-156.
25. N. L. Galinsky, A. Shafiefarhood, Y. Chen, L. Neal and F. Li, *Applied Catalysis B: Environmental*, 2015, **164**, 371-379.
26. V. Galvita, T. Hempel, H. Lorenz, L. K. Rihko-Struckmann and K. Sundmacher, *Industrial & Engineering Chemistry Research*, 2008, **47**, 303-310.
27. T. V. Reshetenko, L. B. Avdeeva, A. A. Khassin, G. N. Kustova, V. A. Ushakov, E. M. Moroz, A. N. Shmakov, V. V. Kriventsov, D. I. Kochubey, Y. T. Pavlyukhin, A. L. Chuvilin and Z. R. Ismagilov, *Applied Catalysis A: General*, 2004, **268**, 127-138.
28. P. H. Bolt, F. H. P. M. Habraken and J. W. Geus, *Journal of Solid State Chemistry*, 1998, **135**, 59-69.
29. L. K. Rihko-Struckmann, M. Wenzel, K. Sundmacher, A. N. V. R. Dharanipragada, H. Poelman, V. V. Galvita and G. B. Marin, *Energy Technology*, 2015, **3**, 1503-1508.
30. J. S. Yoo, A. A. Bhattacharyya, C. A. Radlowski and J. A. Karch, *Industrial & Engineering Chemistry Research*, 1992, **31**, 1252-1258.
31. M. Ji, G. L. Chen, J. H. Wang, X. K. Wang and T. Zhang, *Catalysis Today*, 2010, **158**, 464-469.
32. Q. Imtiaz, M. Broda and C. R. Muller, *Applied Energy*, 2014, **119**, 557-565.
33. I. Adanez-Rubio, P. Gayan, A. Abad, L. F. de Diego, F. Garcia-Labiano and J. Adanez, *Energy & Fuels*, 2012, **26**, 3069-3081.
34. N. L. Galinsky, A. Shafiefarhood, Y. Chen, L. Neal and F. Li, 2015, **164**, 371-379.
35. H. Leion, T. Mattisson and A. Lyngfelt, *International Journal of Greenhouse Gas Control*, 2008, **2**, 180-193.
36. M. Ryden and M. Arjmand, *International Journal of Hydrogen Energy*, 2012, **37**, 4843-4854.
37. M. Ryden, A. Lyngfelt, T. Mattisson, D. Chen, A. Holmen and E. Bjorgum, *International Journal of Greenhouse Gas Control*, 2008, **2**, 21-36.
38. M. Ji, X. Y. Zhang, J. H. Wang and S. E. Park, *J Mol Catal a-Chem*, 2013, **371**, 36-41.
39. J. N. Wang and C. L. Li, *Mater Lett*, 1997, **32**, 223-227.
40. P. Scherrer, *Nachr. Ges. Wiss. Göttingen*, 1918, **2**, 98–100.

41. Y. Ohishi, T. Kawabata, T. Shishido, K. Takaki, Q. H. Zhang, Y. Wang, K. Nomura and K. Takehira, *Appl Catal a-Gen*, 2005, **288**, 220-231.
42. X. Ge, M. S. Li and J. Y. Shen, *Journal of Solid State Chemistry*, 2001, **161**, 38-44.
43. C. H. Bartholomew, *Appl Catal a-Gen*, 2001, **212**, 17-60.
44. P. Datta, L. K. Rihko-Struckmann and K. Sundmacher, *Materials Chemistry and Physics*, 2011, **129**, 1089-1095.
45. T. I. Politova, V. V. Gal'vita, V. D. Belyaev and V. A. Sobyanin, *Catalysis Letters*, 1997, **44**, 75-81.
46. B. R. Cuenya, *Thin Solid Films*, 2010, **518**, 3127-3150.
47. A. S. Madden, M. F. Hochella and T. P. Luxton, *Geochim Cosmochim Ac*, 2006, **70**, 4095-4104.
48. A. Nell, A. Getsoian, S. Werner, L. Kiwi-Minsker and A. T. Bell, *Langmuir*, 2014, **30**, 873-880.
49. S. Roux, A. Bensakhria and G. Antonini, *Int J Chem React Eng*, 2006, **4**.
50. A. Cabello, C. Dueso, F. Garcia-Labiano, P. Gayan, A. Abad, L. F. de Diego and J. Adanez, *Fuel*, 2014, **121**, 117-125.
51. H. H. Dong, M. J. Xie, J. Xu, M. F. Li, L. M. Peng, X. F. Guo and W. P. Ding, *Chem Commun*, 2011, **47**, 4019-4021.
52. I. Baldychev, J. M. Vohs and R. J. Gorte, *Appl Catal a-Gen*, 2009, **356**, 225-230.
53. F. He, Y. G. Wei, H. B. Li and H. Wang, *Energ Fuel*, 2009, **23**, 2095-2102.